


# Scavenging energy from aeroelastic vibrations for hybrid stall control in a fixed-wing micro aerial vehicle

Journal of Vibration and Control  
2023, Vol. 29(21-22) 5195–5207  
© The Author(s) 2022  
Article reuse guidelines:  
[sagepub.com/journals-permissions](https://sagepub.com/journals-permissions)  
DOI: 10.1177/10775463221132596  
[journals.sagepub.com/home/jvc](https://journals.sagepub.com/home/jvc)  


Ali Esmaeili<sup>1</sup> , Hugo Emanuel da Costa Delgado<sup>2</sup> and Joao Manuel Melo Sousa<sup>2</sup> 

## Abstract

Scavenging energy from aeroelastic vibrations was considered for a self-powered hybrid passive-active stall control system intended to improve the aerodynamic performance of fixed-wing micro aerial vehicles without exhausting available batteries. It was found that the passive component of the system generates intense streamwise vortices, which give rise to vortex-induced vibrations. Measured frequency response functions indicated accelerations in a wing prototype up to 0.1 g at relatively low frequencies, when it was operated at simulated flight conditions in a wind tunnel. Aiming to use this resource for additional power, a piezoelectric energy harvesting device was installed inside the wing and tuned for resonant response. Two electromechanical modeling approaches for the piezoelectric harvester were investigated, namely, an analytical model and finite elements simulations. A comparison with experimental results has shown that the latter approach is better equipped to deal with advanced designs, yielding accurate predictions in the present study. Extracted power and generated voltage were quantified as a function of the electric loading resistance. The reported data demonstrated that the proof of concept was achieved, so that a lightweight, low-consumption actuator for the active component of the stall control system can be powered by the energy of structural vibrations.

## Keywords

piezoelectric energy harvester, aeroelastic vibrations, modal analysis, micro aerial vehicle, stall control

## 1. Introduction

During the last decade, micro air vehicles (MAVs) have seen an exponential growth in interest and use for many practical applications. On the basis of recent advancements in propulsion, flight control, and sensors technologies, MAVs can be designed with a typical wing span of 5–25 cm, which makes them at least 10 times smaller than the smallest unmanned air vehicles (UAVs). The combination of small size and low flight velocities of MAVs yields that they operate in the low Reynolds number regime ( $Re < 200,000$ ), for which the aerodynamics has not been well established yet. In this flow regime, the prevalent aerodynamic dead-lock concerns the ability to generate a sufficiently high lift-to-drag ratio, given the tendency of laminar boundary layers to separate at relatively low incidence angles (Jabbari et al., 2021a), and the occurrence of early aerodynamic stall (Mueller and DeLaurier, 2003). Consequently, these undesirable phenomena raise the need for passive or active flow control, and it is perhaps not surprising that researchers have sought inspiration from nature and biomimetics (Jabbari et al., 2021b).

Biomimetic inspiration from the pectoral flippers of humpback whales (Fish and Battle, 1995) was behind the use of a wing with a scalloped leading-edge, resulting in the generation of intense streamwise vortices (Câmara and Sousa, 2013) (Esmaeili et al., 2018), as illustrated in Figure 1. These vortices re-energize low-velocity regions occurring in the air flow around the wing when it is subjected to aerodynamic stall (Delgado et al., 2014), but also create flow-induced vibrations, and have a detrimental effect on the wing performance at pre-stall conditions

<sup>1</sup>Engineering Faculty, Mechanical Engineering Department, Ferdowsi University of Mashhad, Iran

<sup>2</sup>IDMEC, Universidade de Lisboa Instituto Superior Técnico, Portugal

Received: 8 April 2022; revised: 13 August 2022; accepted: 24 September 2022

### Corresponding author:

A Esmaeili, Engineering Faculty, Mechanical Engineering Department, Ferdowsi University of Mashhad, Azadi Square, Ferdowsi university, Mashhad, Khorasan 9177948974, Iran.  
Email: [aliesmaeili@ferdwosi.um.ac.ir](mailto:aliesmaeili@ferdwosi.um.ac.ir)

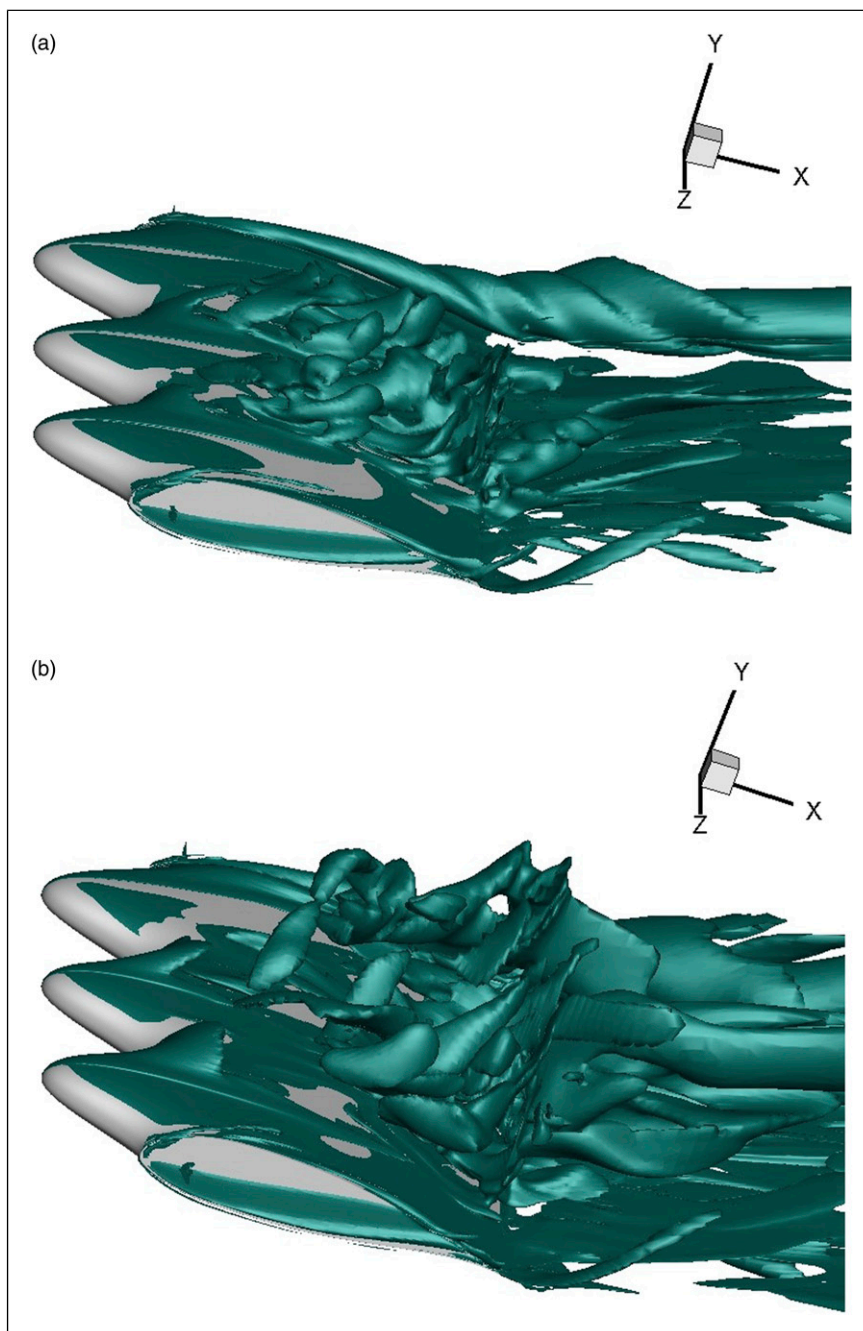


**Figure 1.** Streamwise vortices in the air flow (passive stall control mechanism) generated by the scalloped leading-edge of the wing at (a) pre-stall and (b) post-stall conditions.

(Guerreiro and Sousa, 2012). A hybrid passive-active stall control solution has therefore been sought, where a minimal amount of energy would be required to power an active control component solely intended to minimize the aforementioned aerodynamic losses. In this case, the availability of additional energy sources becomes crucial, as the utilization of heavier batteries to power auxiliary systems further reduces the payload capacity of a MAV. Increased endurance and flight range are also desirable in most

missions of such vehicles. However, even if this goal is not achieved via the use of a particular energy harvesting technology, the readiness of distributed sources of small amounts of energy may still be advantageous for special design solutions (Martos et al., 2015).

Other researchers have also shown that MAVs are subjected to unsteady aerodynamic loads during their flight, hence giving rise to aeroelastic vibrations (Xiang et al., 2015) (dos Santos et al., 2019). The transformation of these

into a useable form of energy has been the subject of many studies in the field of Aerospace (Li et al., 2016). Nevertheless, due to claimed advantages such as high-power density, architectural simplicity, and scalability, piezoelectric energy harvesting has established itself as the preferred choice in the field (Toprak and Tigli, 2014) (Meshki et al., 2020). In the design and optimization of these scavengers of vibration energy, numerical simulations have been widely employed (Esmaeili and Sousa, 2017). An electromechanical model is thus required and a variety of approaches has been considered. A simplification into a topology of discrete entities approximating the behavior of the spatially distributed system is applied when lumped parameter models are used (Roundy et al., 2003) (Dutoit et al., 2005). However, accurate predictions require distributed parameters modeling, directly or indirectly involving the Rayleigh–Ritz method and the extended Hamilton’s principle (along with energy considerations) to derive the governing equations (DuToit and Wardle, 2007) (Elvin and Elvin, 2009). Analytical solutions with closed-form expressions can be obtained in the foregoing case by assuming appropriate eigenfunctions (Erturk and Inman, 2009) and, despite its higher computational cost, finite elements modeling also provides an alternative way to formulate and solve this type of electromechanical problems (De Marqui Junior et al., 2009) (Fatehi et al., 2021).

It is also noteworthy that piezoelectric energy harvesting systems have previously been designed and bench-tested specifically for use in fixed-wing MAV (Anton et al., 2010) (Anton et al., 2012), for example, with the objective of locally powering low-consumption electronics. However, reports of experimental testing in real or simulated flight conditions are still very scarcely found in the literature and more proofs of concept (Anton and Inman, 2008) are instrumental to advance this technology.

In the present study, a flying wing MAV configuration incorporating a piezoelectric energy harvester is tested in a wind tunnel, and supporting numerical simulations are also conducted. The main objective of this study is to develop a proof of concept for the use of a piezoelectric device to scavenge energy from aeroelastic vibrations, aimed at the novel application of hybrid passive-active stall control in a fixed-wing MAV. Accordingly, the wing was designed to include a leading-edge modification with biomimetic inspiration, primarily allowing passive stall control via the formation of streamwise vortices. However, these intense flow structures not only energize the boundary layer over the wing but also generate flow-induced vibrations with a strong potential for energy harvesting to power the intermittent use of chip-scale active stall control devices as well. To the authors’ best knowledge, it is the first time that the concept of combining energy harvesting from aeroelastic vibrations to achieve hybrid passive-active stall control in a fixed-wing MAV is proposed and systematically explored employing both experimental work and numerical

simulations. A secondary goal of this work is to validate an electromechanical modeling approach for the design of piezoelectric energy harvesters with the ability to cope with the various complexities of advanced solutions.

The prototype and specific wing features are described in section 2. The instrumentation used in wind tunnel testing is presented in section 3, followed by vibration measurements and a discussion of the outcome of the modal analysis. In section 4, details of the electromechanical models employed to study the performance of the piezoelectric energy harvester are provided. The tuning procedure of this experimental device is the subject of section 5. The results of the experiments and the modeling validation for energy scavenging are given in section 6. Finally, section 7 summarizes the main findings of this investigation.

## 2. Micro air vehicle wing prototype

The aerodynamic characteristics of the wing geometry employed in the present study were extensively studied in a previous experimental investigation (Guerreiro and Sousa, 2012), using a series of (rigid) Duraluminium models in the optimization of the passive stall control mechanism. The scalloped leading-edge depicted in Figure 1 was crafted based on a sinus function, which locally elongates and shortens the chord of a baseline wing section corresponding to the NASA LS(1)-0417 airfoil, while keeping the mean chord value unchanged. Best aerodynamic performance was reported to be obtained for an amplitude and wavelength of the sinus function of 6% and 12% of the chord, respectively, when a wing with of aspect ratio  $AR = 1.5$  was considered.

Based on the above-mentioned information, an MAV wing prototype was built in thermoformed Acrylonitrile Butadiene Styrene (ABS) plastic—a polymeric material—using additive manufacturing. A smooth surface finish was obtained using progressively finer sandpaper, down to P240. The ABS wing prototype structure basically consisted of a 2-mm-thick skin, one 3-mm-thick main spar, and several 2-mm-thick perforated ribs, as illustrated in Figure 2. In order to facilitate the access to the interior space, a large part of the lower surface skin was converted into two separate removable panels (not shown in Figure 2) also manufactured in ABS plastic. When assembled together, beeswax was used to fill any gaps and provide adequate air sealing. The total weight of the complete assembly, with a mean chord  $c = 232$  mm and a full span  $cAR = 348$  mm, was 470 g.

## 3. Vibrations measurements

A series of tests were made to measure the vibrations in the ABS wing prototype, when subjected to simulated flight conditions inside a wind tunnel. This facility achieves

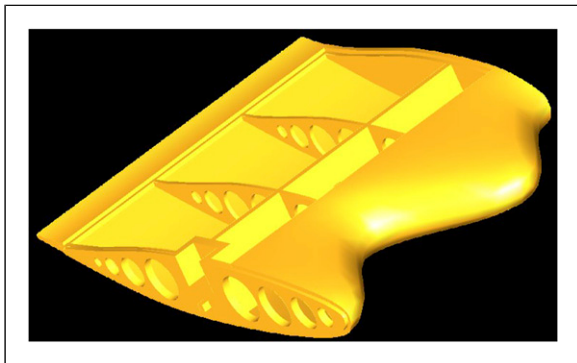


**Figure 2.** Drawing of the starboard side of the ABS wing prototype, with the corresponding lower surface service panel removed, and illustrating its main structural elements.

a maximum wind velocity  $U = 10 \text{ ms}^{-1}$ , with a test section of  $0.8 \times 1.2 \text{ m}^2$ , and it was operated at a constant Reynolds number  $Re = Uc/\nu = 140,000$  (where  $\nu$  denotes the kinematic velocity of the air) during the whole experimental campaign. The reader is referred to (Guerreiro and Sousa, 2012) for a full description of the wind tunnel features. Aiming to better characterize the nature of the vibrations, both dynamic accelerations and velocities were measured using accelerometers and a laser-Doppler vibrometer, respectively. Data acquisition was carried out with a 4-channel OROS compact analyzer (model OR34) interfaced with a digital laptop running OROS NVGate software version 7. A data rate of 1600 samples per second was used, with a frequency range set to 0–500 Hz and a 50% overlapping. Aiming to minimize the noise level in the data (Ewins, 2000), Frequency Response Functions (FRFs) were averaged in time during up to 15 min. A schematic of this experimental setup is depicted in Figure 3 and additional details about both apparatuses are provided in the next subsections.

### 3.1 Accelerometers

Initial modal analysis measurements were carried out using three Brüel and Kjær type 4507 accelerometers, one for each of the axes of the frame of reference shown in Figure 3. These were installed inside the ABS wing prototype as illustrated in Figure 4(a). The accelerometers corresponding to the  $X$ - and  $Z$ -axis were directly connected to the compact analyzer. Conversely, the much weaker signal generated by the  $Y$ -axis accelerometer required the additional use of a Brüel and Kjær type 2635 charge amplifier, which is the most adequate choice when measuring low frequencies using rather long connecting cables (3 m in the present case). It is well known that adding mass to a structure is likely to alter its vibrational characteristics and, consequently, lead to

inaccurate data and analysis. However, the total weight of the three accelerometers was less than 5% of the weight of the ABS wing prototype.

### 3.2 Laser-Doppler vibrometer

Aiming to verify the results of the modal analysis obtained by the use of the accelerometers, as well as the origin of the vibrations, additional measurements were subsequently performed employing a laser-Doppler vibrometer. Simultaneous velocity responses in the  $Z$ -axis direction, from both the skin of the ABS wing prototype (laser A) and at the joint of the support strut (laser B), were measured using a dual-channel Polytec® vibrometer basically consisting of a laser generator model OFV-518 and a controller model OFV-2802i. Target reflective tape 3M Scotchlite™ was used at the location of each of the two laser spots, as shown in Figure 4(b).

### 3.3 Results of the modal analysis

The first results of the modal analysis were obtained with the wing placed in the wind tunnel at two different angles of attack, namely,  $\alpha = 15 \text{ deg}$  (pre-stall condition) and  $20 \text{ deg}$  (post-stall condition), as shown in Figure 5(a) for the  $Z$ -axis accelerometer only. The measured FRF using the  $X$ - and  $Z$ -axis accelerometers are compared in Figure 5(b). Accelerations from the  $Y$ -axis accelerometer were omitted in the foregoing plot because these were typically two to three orders of magnitude lower. Apart from the directional differences in compliance of the structure, this observation was not surprising as the  $Y$ -axis corresponds to the spanwise direction of the ABS wing prototype, hence expectedly less responsive to the aeroelastic vibrations eventually generated by streamwise vortices. Irrespective of the wing incidence, a well-defined fundamental frequency  $f_1 = 17.6 \text{ Hz}$  was detected, accompanied by several harmonics. However, the largest acceleration was measured at a frequency  $f_2 = 2f_1 = 35.3 \text{ Hz}$  for the  $Z$ -axis, at  $\alpha = 20 \text{ deg}$ , rising to approximately  $0.1 \text{ g}$ . The corresponding value obtained at  $\alpha = 15 \text{ deg}$  was about 20% lower.

The spectral coherence observed together with the fact that the measured accelerations increased with the angle of attack are consistent with vortex-induced vibrations. Moreover, the low value of the fundamental frequency  $f_1$  results in a Strouhal number  $f_1 c \sin\alpha/U \approx 0.15$ , which lies within the typical range for vortex shedding from airfoils and finite wings at incidence  $\alpha$  in a free stream with velocity  $U$  (Colonius and Williams, 2011). The FRF of velocity in the  $Z$ -axis obtained from the laser-Doppler vibrometer and reported in Figure 6 further substantiate this idea, as much lower velocities were measured at the joint of the support strut (laser B) than on the skin of the ABS wing prototype (laser A), especially in the low-frequency range. Although the use of a strut to support the wing inside the wind tunnel

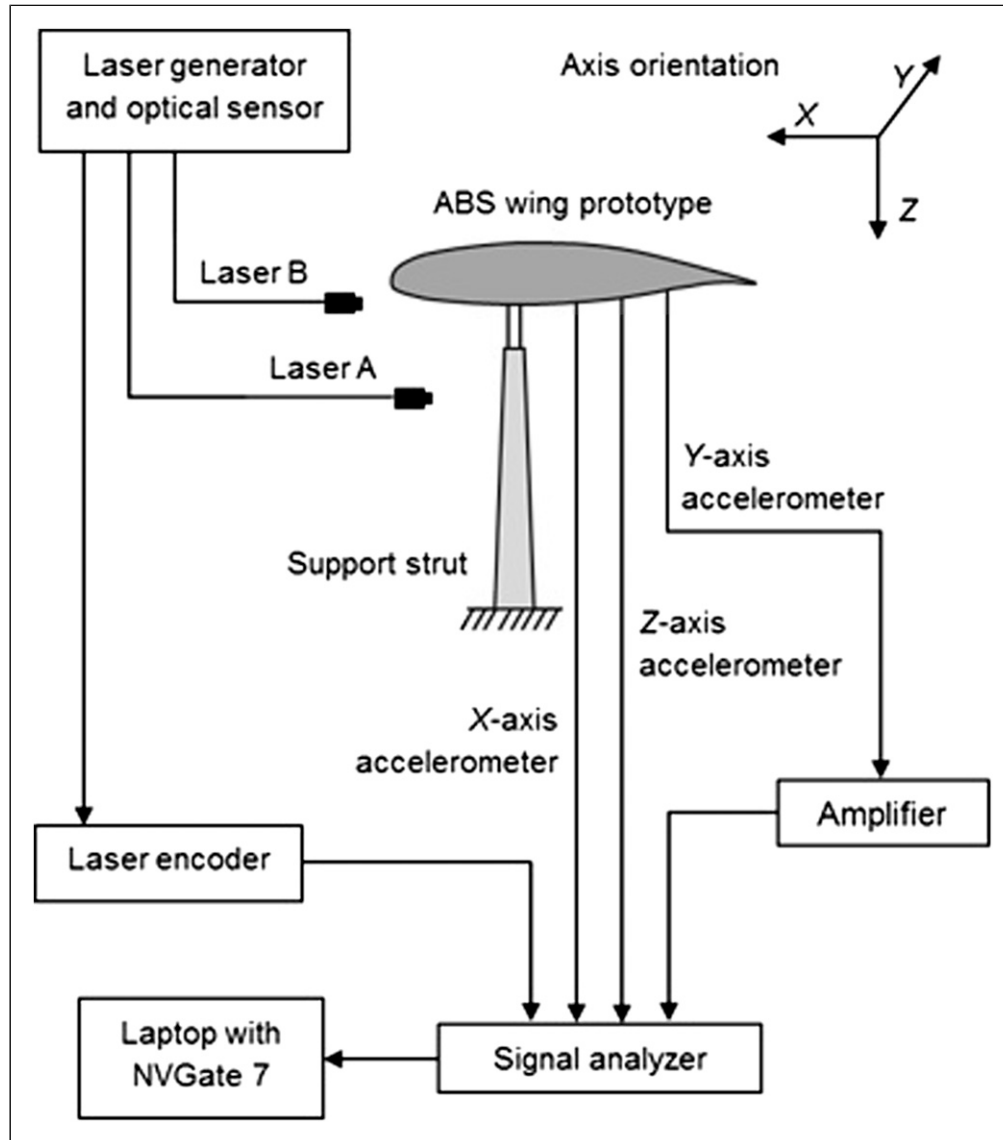


**Figure 3.** Schematic of the experimental setup for vibrations measurements.

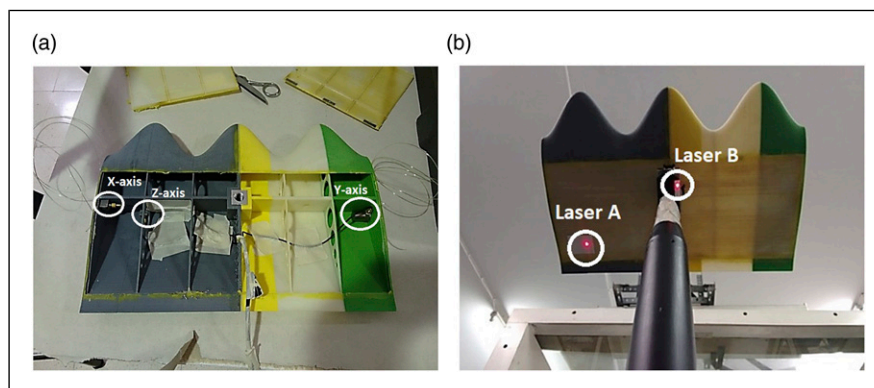


**Figure 4.** Locations of vibration measurements: (a) accelerometers installed inside the ABS wing prototype; (b) laser spots from the vibrometer.

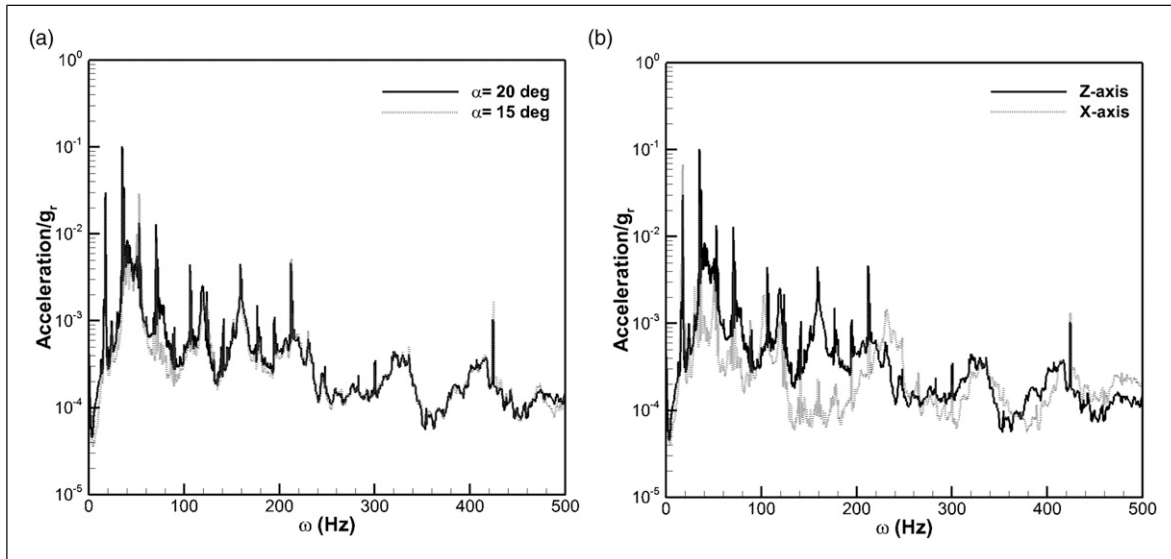


**Figure 5.** Frequency response functions of acceleration obtained using the accelerometers: (a) Z-axis for  $\alpha = 15$  deg and 20 deg; (b) X- and Z-axis at  $\alpha = 20$  deg.

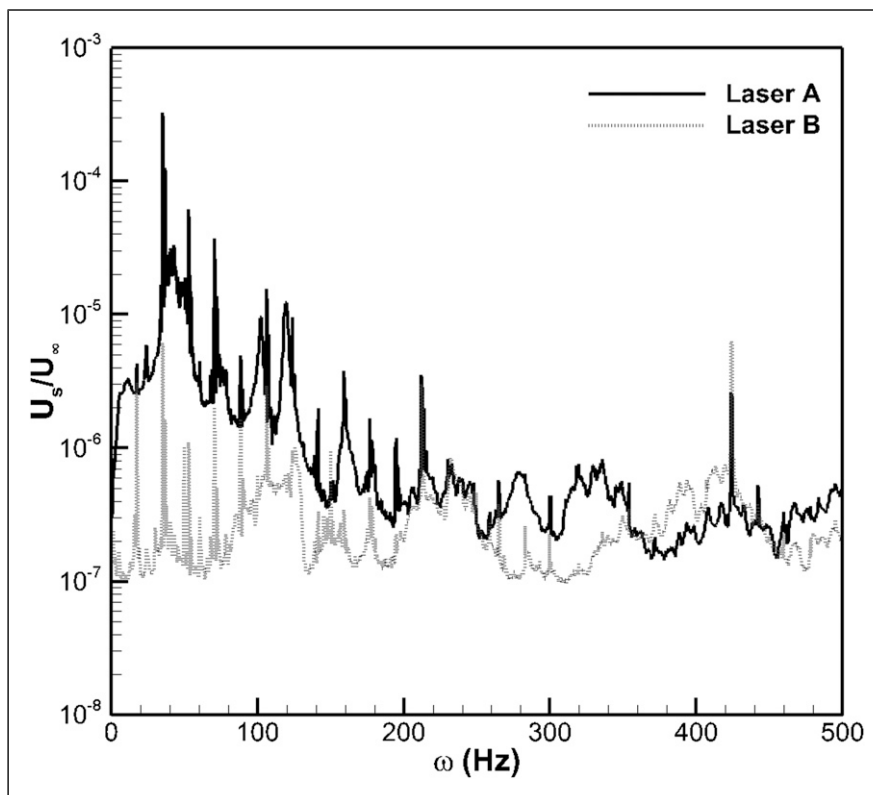


**Figure 6.** Frequency response functions of velocity of the skin of the ABS wing prototype (laser A) and at the joint of the support strut (laser B) obtained using the laser-Doppler vibrometer.

is not the most desirable setup to carry out a modal analysis of the wing structure, as the non-negligible compliance of the support and the constraint of degrees of freedom may interfere with the intended study, this solution was chosen

due to the unsteady forces imposed by the wind. Nevertheless, the present results seem to indicate that the vibrations are essentially transmitted to the support strut by the wing and not the reverse.

## 4. Electromechanical modeling

As explained earlier, the main objective of this study was to investigate the possibility of scavenging energy from the aeroelastic vibrations characterized in the previous section, employing a cantilever beam type of piezoelectric energy harvester. For this purpose, a commercially available device (see Section 5) will be installed and tested inside the ABS wing prototype. More optimized solutions can certainly still be obtained by designing a device with the specific purpose of embedding it in structural elements of the wing. However, this was not sought at this stage and, conversely, a procedure leading to simpler implementation and testing was preferred for the intended proof of concept.

### 4.1 Constitutive relations

In the presence of relatively low excitation amplitudes, the coupled electromechanical behavior of the beam is governed by the linear-elastic constitutive relations for the inverse piezoelectric effect, connecting the developed electric displacement  $\mathbf{D}$ , applied electric field  $\mathbf{E}$ , applied strain  $\mathbf{S}$ , and developed mechanical stress  $\mathbf{T}$ . If the transducer is considered to operate in the transverse mode {3–1}, with the assumptions of plane stress and transverse bending only, the electromechanical model relating the aforementioned vector quantities simply reduces to

$$\begin{Bmatrix} T_1 \\ D_3 \end{Bmatrix} = \begin{bmatrix} c_{11}^E & -e_{31} \\ e_{31} & \varepsilon_{33}^S \end{bmatrix} \begin{Bmatrix} S_1 \\ E_3 \end{Bmatrix} \quad (1)$$

thus involving, in this case, the use of the elastic compliance  $s_{11}^E$  and the strain coefficient  $d_{31}$  in the well-known one-dimensional beam relations:  $c_{11}^E = 1/s_{11}^E$ ,  $e_{31} = d_{31}/s_{11}^E$ , and  $\varepsilon_{33}^S = \varepsilon_{33}^T - d_{31}^2/s_{11}^E$ .

### 4.2 Analytical model

A closed-form analytical model for a base-excited cantilever beam type of piezoelectric energy harvester may be obtained, as described, for example, by (Dutoit et al., 2005), making use of Euler–Bernoulli theory and Hamilton’s Principle for deformable bodies. According to the former, the equation of motion for a beam subjected to a transverse base excitation displacement  $u_B(t)$ , which is a function of time  $t$  only, may be expressed as

$$\frac{\partial^2 \Phi}{\partial r^2}(r, t) + \rho A(r) \frac{\partial^2 u}{\partial t^2}(r, t) = -\rho A(r) \frac{\partial^2 u_B}{\partial t^2}(t) \quad (2)$$

where  $\Phi(r, t)$  stands for the bending moment and  $\rho A(r)$  is the mass per unit length. The absolute displacement of the beam  $u(r, t)$  is given in terms of the base displacement and the beam transverse displacement response, as simple

bending deflection is considered. On the other hand, according to the generalized Hamilton’s principle for an electromechanical system, neglecting magnetic terms and defining kinetic  $E_k$ , internal potential  $E_u$ , and electrical  $E_e$  energies, together with the external work  $W$ , one may write

$$\int_t^{t+\Delta t} [\delta(E_k + E_u + E_e) + \delta W] dt = 0 \quad (3)$$

where  $\delta$  denotes the first variation of the function in Variational Calculus. The various terms in equation (3) may be formulated as a function of relative displacement, and electric potential (assumed to be constant across the piezoelectric layers), introducing also the constitutive relations provided in the previous subsection. Full details can be found in the study conducted by Dutoit et al. (2005).

Following the Rayleigh–Ritz procedure, the displacement of the beam is written as the sum of  $N$  individual mode shapes  $\varphi_N$  (as a function only of the axial position  $x$  of the neutral axis in this case) multiplied by the generalized mechanical coordinate  $r(t)$ . The general bending mode shape for a clamped beam is given by

$$\varphi_N = A[(\cosh \beta_N x - \cos \beta_N x) - \alpha(\sinh \beta_N x - \sin \beta_N x)] \quad (4)$$

where  $A$  is a single arbitrary constant and  $\beta_N$  denotes the resonance modes associated to the natural frequencies of the beam. Both the modes  $\beta_N$  and the coefficient  $\alpha$  are calculated in this case from a determinant solution obtained by expressing the boundary conditions of the beam in matrix form.

As shown, for example, by DuToit and Wardle (2007), when considering a single beam mode  $\varphi_1$  (i.e., approximating the infinite-degree-of-freedom mechanical system as a single-degree-of-freedom system), a pair of coupled scalar ordinary differential equations result for the generalized mechanical displacement  $r$  and the developed voltage  $v$ , yielding

$$\ddot{r} + 2\zeta\omega_1\dot{r} + \omega_1^2 r - \frac{\theta}{M}v = -\frac{F}{M}a_B \quad (5)$$

$$\theta\dot{r} + C_p\dot{v} + \frac{1}{R}v = 0 \quad (6)$$

where  $\zeta$  stands for the mechanical damping ratio,  $\omega_1 = \sqrt{K/M}$  corresponds to the angular frequency associated to the first beam mode  $\varphi_1$ ,  $a_B$  denotes the base acceleration,  $F$  represents the inertial load for a beam of uniform cross-section,  $M$ ,  $C_p$ , and  $\theta$  indicate the mass, capacitive, and coupling coefficients, respectively, and  $R$  is the electric load resistance, as given in (Dutoit et al., 2005). It must also be noted that, according to this

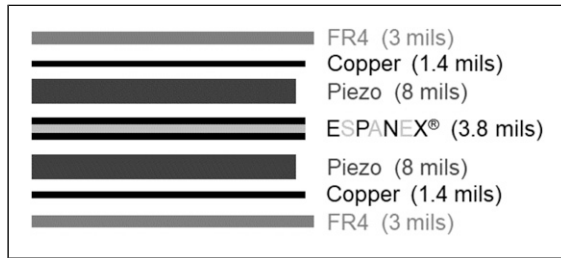


**Figure 7.** Multilayer structure of the piezoelectric energy harvester used. The thickness of each layer is indicated in thousands of an inch (1 mil = 0.0254 mm) and Epoxy has been used in the packaging process.

formulation, actual displacements of the beam are  $u = r\phi_1$ .

Using Laplace transforms, equations (5) and (6) can be evaluated to determine duly normalized (using the input force  $Fa_B$ ) magnitudes of displacement, voltage, and extracted electrical power by the following algebraic expressions:

$$\langle r \rangle = \frac{1}{K} \sqrt{\frac{1 + (\gamma\Omega)^2}{\chi_1^2 + \chi_2^2}} \quad (7)$$

$$\langle v \rangle = \frac{1}{|\theta|} \frac{\gamma\kappa^2\Omega}{\sqrt{\chi_1^2 + \chi_2^2}} \quad (8)$$

$$\langle P \rangle = \frac{\omega_1}{K} \frac{\gamma\kappa^2\Omega^2}{\chi_1^2 + \chi_2^2} \quad (9)$$

with factors  $\chi_1 = 1 - (1 + 2\gamma\zeta)\Omega^2$  and  $\chi_2 = [2\zeta + \gamma(1 + \kappa^2)]\Omega - \gamma\Omega^3$ , where  $\gamma = \omega_1 RC_p$ ,  $\kappa = \theta/\sqrt{KC_p}$  and  $\Omega = \omega/\omega_1$  physically represent a dimensionless time constant, an electromechanical coupling coefficient for the system, and the ratio between the excitation (angular) frequency  $\omega$  and the mode of oscillation  $\omega_1$ , respectively.

### 4.3 Finite elements model

A finite elements (FE) formulation for the electromechanical problem under consideration may be derived via the application of the variational principle together with an appropriate discretization procedure. For this purpose,

$$\begin{Bmatrix} \mathbf{M} & \mathbf{0} \\ \mathbf{0} & \mathbf{0} \end{Bmatrix} \begin{Bmatrix} \ddot{\mathbf{u}} \\ \ddot{\mathbf{v}} \end{Bmatrix} + \begin{Bmatrix} \mathbf{C} & \mathbf{0} \\ \mathbf{0} & \mathbf{C}_d \end{Bmatrix} \begin{Bmatrix} \dot{\mathbf{u}} \\ \dot{\mathbf{v}} \end{Bmatrix} + \begin{Bmatrix} \mathbf{K} & \mathbf{K}_k \\ \mathbf{K}_k^t & \mathbf{K}_d \end{Bmatrix} \begin{Bmatrix} \mathbf{u} \\ \mathbf{v} \end{Bmatrix} = \begin{Bmatrix} \mathbf{F} \\ \mathbf{L} \end{Bmatrix} \quad (10)$$

nodal solution variables and element shape functions are established over each domain element. Classical relations may be used to relate the strain  $\mathbf{S}$  with the displacement  $\mathbf{u}$ , as well as the electric field  $\mathbf{E}$  with the electric potential  $\mathbf{v}$ , so

that the following set of coupled matrix equations for each domain element is obtained:

where  $\mathbf{M}$ ,  $\mathbf{K}$ ,  $\mathbf{C}$ , and  $\mathbf{C}_d$  represent the mass, stiffness, and structural and dielectric damping matrices, respectively,  $\mathbf{K}_d$  and  $\mathbf{K}_k$  denote the dielectric conductivity and piezoelectric coupling matrices, respectively, and  $\mathbf{F}$  and  $\mathbf{L}$  stand for structural and electric load vectors, respectively.

In the present investigation, each node point of the FE modeling mesh has four degrees of freedom (three displacement components and voltage). The steady-state response of the structure to a sinusoidal varying load was determined by harmonic analysis and transient effects at the beginning of the vibrations were ignored. More details concerning the numerical solution of equation (10) for the cantilever beam type of energy harvester are given in subsection 6.2.

## 5. Piezoelectric energy harvester

### 5.1 Original device characteristics

A Voltare™ piezoelectric energy harvester model V21 B (Midé Technology Corporation, 2013a) developed by Midé Technology Corporation was selected due to its low-cost and robustness. Consisting in a bimorph configuration, this harvester is formed by seven layers packaged together in a sandwich construction using Epoxy. As illustrated in Figure 7, the substrate is made of ESPANEX® which is a flexible double-sided Copper clad polyimide (dielectric) laminate also used for circuitry (i.e. incorporating the inner electrodes), surrounded by the two layers of the piezoceramic material CTS-3195HD, followed by the two remaining Copper electrodes, and encapsulated by the high-pressure thermoset plastic laminate FR4, which is mainly used as an electrical insulator. A thorough listing of the properties and characteristics of the materials used was made available by the manufacturer (Midé Technology Corporation, 2013b), but a summary is also presented here in Table 1. Standard properties were considered for Copper.

### 5.2 Device tuning procedure

It was demonstrated in Section 3 that the frequencies associated to the larger accelerations produced by vortex-

induced vibrations in the wing are lower than typical natural frequencies of this type of energy harvesters, generally above 100 Hz. Unfortunately, the selected device is not an exception, exhibiting a natural frequency  $f_n = 110$  Hz as



**Table 1.** Summary of the properties of materials used in the piezoelectric energy harvester (Midé Technology Corporation, 2013b).

FR4	Epoxy		ESPANEX®		
Young's modulus (GPa)	23.4	Shear strength (MPa)	37.23	Tensile modulus (MPa)	4500
Poisson's ratio	0.14	Density (kg/m <sup>3</sup> )	730	Tensile elongation (%)	49.3
Density (kg/m <sup>3</sup> )	1920			Density (kg/m <sup>3</sup> )	1420
Piezoceramic CTS-3195HD					
Coupling coefficient, $k_{31}$		0.36	Elastic compliance, $s_{33}^E$ (m <sup>2</sup> /N)		$18.8 \times 10^{-12}$
Coupling coefficient, $k_{33}$		0.72	Elastic compliance, $s_{11}^E$ (m <sup>2</sup> /N)		$16.4 \times 10^{-12}$
Density (kg/m <sup>3</sup> )		7800	Relative permittivity, $\epsilon_{33}^T$		1700
Strain constant, $d_{31}$ (C/N)		$-190 \times 10^{-12}$	Relative permittivity, $\epsilon_{33}^S$		830
Strain constant, $d_{33}$ (C/N)		$390 \times 10^{-12}$			

**Table 2.** Dimensions of the Volture™ V21 B harvester (active part) and tip plate.

Dimensions	V21 B	Tip plate
Length (mm)	35.56	26.0
Width (mm)	14.48	8.0
Thickness (mm)	0.787	1.0

indicated by the manufacturer (Midé Technology Corporation, 2013a, 2013b). Knowing in advance that the power harvested decays sharply even with a moderate departure of the operating frequency with respect to  $f_n$ , tuning the device for this frequency is mandatory. This may be simply achieved by introducing a tip mass. However, a preliminary analysis demonstrated that the weight of the tip mass required in this case would be prohibitively large. Hence, it was decided to couple the aforementioned procedure with a modification to the original device, including the use of a steel tip plate together with a tip mass with (optimum) characteristics to be determined. Table 2 lists the dimensions of the Volture™ V21 B and the additional tip plate, which produced an effective increase in the length of 20 mm.

## 6. Experiments and modeling validation for energy scavenging

### 6.1 Installation and preliminary testing

Based on the vibrations measurements previously carried out, a single piezoelectric energy harvester was installed inside the ABS wing prototype approximately at the same position of the Z-axis accelerometer used in Section 3, carefully following the indications of the manufacturer regarding clamping (Midé Technology Corporation, 2013a, 2013b). The electric loading was varied by the use of a variable resistor, allowing a circuit impedance range of

10 k $\Omega$ –0.8 M $\Omega$ . Resistances were measured using a standard multimeter Yokagawa model 7551, with an accuracy of 0.02%, a maximum resolution of 1  $\Omega$  and an internal impedance of 1 M $\Omega$  in a series connection. The same instrument was later also used to measure voltage amplitudes of the electric signal generated by the energy harvester in operation, with the same level of accuracy and a maximum resolution of 0.1 mV. When required, this signal was monitored as well, employing a digital oscilloscope Tektronix model TDS 320.

A pair of electrodes plus a piezoelectric layer is denoted here as an element. As the selected harvester includes two elements (marked 1 and 2), the connection between these can be made in series or parallel. Depending on the chosen connection, electromechanical modeling will also change in accordance. For a series connection, the two elements are poled in opposite directions as shown in Figure 8(a), such as the strains produced by bending above and below the neutral axis of the harvester beam generate electric fields flowing in the same direction. Hence, for this circuit, the total voltage  $v$  is the sum of voltages  $v_1$  and  $v_2$ . On the other hand, the parallel connection depicted in Figure 8(b) requires that both elements are poled in the same direction, with corresponding changes in circuitry.

Preliminary tests were performed, with a series connection of the piezoelectric wafers of the device, in order to determine the weight of the lead tip mass to be used in the tuned configuration. Maximum extracted power for the simulated flight conditions described earlier in Section 3 was obtained for a resistance of approximately 230 k $\Omega$ . Table 3 lists the resulting power values for different tip masses, varying discretely in increments of 0.25–0.50 g. In accordance to these data, a tip mass of only 4.5 g was subsequently used in the remaining experiments; hence, its impact on the static and aeroelastic behavior of a kilogram-size vehicle is expected to be negligible. The tuned device is shown in Figure 9(a) with the tip mass attached and in

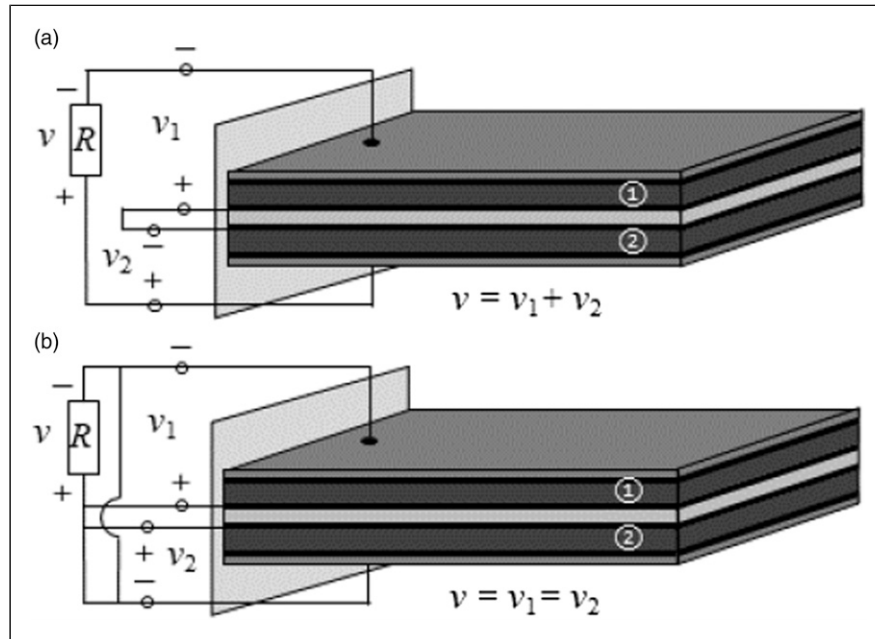


**Figure 8.** Schematics of electrical connections between elements in the symmetric bimorph device: (a) for series electrical connection; (b) for parallel electrical connection.

**Table 3.** Determination of (optimum) tip mass for device tuning.

Tip mass (grams)	Power ( $\mu\text{W}$ )
3.00	0.70
3.50	1.95
4.00	6.69
4.25	18.27
4.50	22.40
4.75	21.04
5.00	12.86
5.50	5.26

Figure 9(b) after installation. An additional experiment was conducted with the aim of determining the value of the damping ratio  $\zeta$  appearing in equation (5). These measurements were repeated several times to improve the accuracy of the estimate and the ensemble averaged value  $\zeta = 0.0245$  was obtained.

## 6.2 Extracted power and voltage

The extracted power and voltage generated by the energy harvester were measured as a function of the electric load resistance, for both series and parallel connections of the piezoelectric wafers, with the ABS wing prototype subjected to simulated flight conditions characterized by  $Re = 140,000$  and  $\alpha = 20$  deg. The experimental data were also compared with the results of the numerical modeling (series connection only) from both the analytical model and the FE

simulations, aiming to assess their capabilities for future use in design at more advanced stages.

Numerical results employing both modeling approaches were obtained considering a base excitation of the beam, expressed in terms of an acceleration along the Z-axis, with an amplitude of 0.1 g and a frequency of 35.3 Hz, corresponding to the most energetic mode of the aeroelastic vibrations in the wing (see, for example, Figure 5 in subsection 3.3). The FE analysis of the energy harvester was performed using ANSYS® Academic software v. 14.5 in Workbench environment, with direct coupled-field analysis and a coupled physics circuit simulation. The geometry of the tuned device illustrated in Figure 9(a) was created using ANSYS® DesignModeler. In addition, defining the piezoelectric material properties and the connections between the various layers depicted in Figure 7 (see subsection 5.1), as well as setting the correct poling direction, was accomplished by adding command macros in ANSYS® APDL language. A modal analysis allowed to confirm that the mechanical design was accurate, as the frequency corresponding to the first mode shape (simple bending deflection) obtained for the cantilever beam matched the excitation frequency exactly. In order to obtain the FE solution, substrate layers, electrodes, and tip mass were modeled using high-order, three-dimensional 20-node hexahedral elements (SOLID186) with three translational degrees of freedom in each node, whereas the piezoelectric layers employed three-dimensional 20-node piezoelectric elements (SOLID226) with an additional degree of freedom for voltage in each node. Finally, a resistor element (CIRCU94) was also defined for the connection of the two piezoelectric

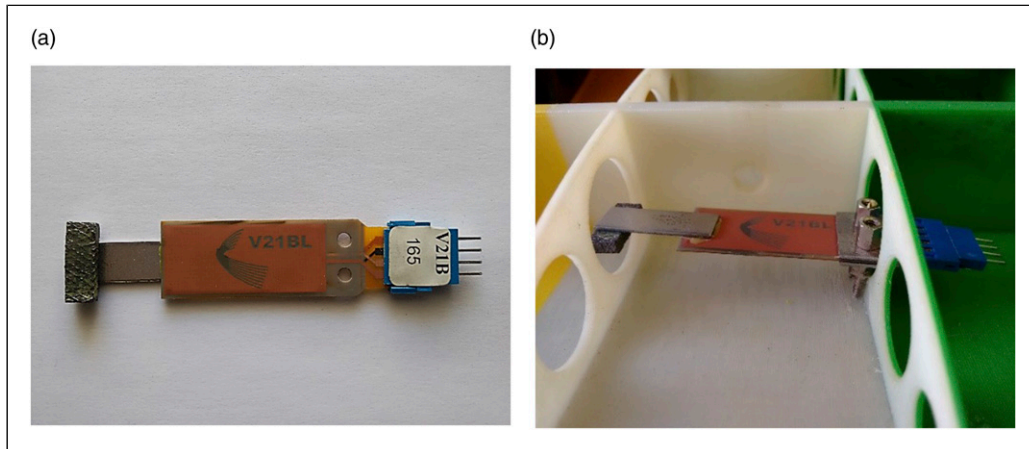


**Figure 9.** Piezoelectric energy harvester after the tuning procedure: (a) device with lead tip mass attached; (b) device clamped to the wing structure.

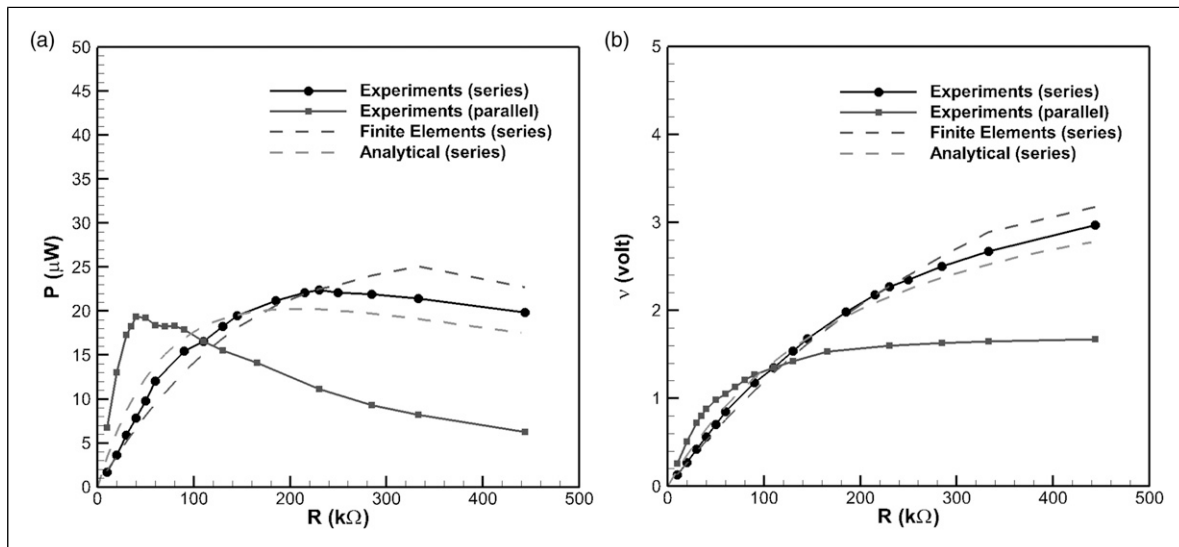


**Figure 10.** Measured and predicted electric output: (a) extracted power; (b) generated voltage.

wafers of the energy harvester in series or parallel, thus allowing a quantification of the electric output.

The measured values of extracted power and voltage generated by the piezoelectric energy harvester are shown in Figure 10(a) and (b), respectively. Data for both series and parallel connections are presented, indicating that for the former case, the power peaks at 230  $k\Omega$  (as mentioned earlier in subsection 6.1), and for the latter case, this occurs at an electric loading resistance as low as 40  $k\Omega$ . Although the same value for the peak power output was expected irrespective of the type of connection, a slightly lower maximum was obtained for a parallel connection. An explanation may perhaps be found on the larger relative errors at low electric loading, resulting from the added inductance to the circuit due to the coil geometry of the variable resistor employed in the experiments. Regardless of the foregoing

discrepancy, these magnitudes of extracted power are consistent with prior data for piezoelectric energy harvesters, typically in the microwatt to milliwatt range (Anton and Sodano, 2007). As continuous operation would not be required, the minute amount of harvested energy is still expected to allow the implementation of a lightweight, low-consumption actuator for intermittent use of the active component of the hybrid (passive-active) stall control system, such as a chip-scale electrodynamic synthetic jet actuator (Sawant et al., 2015).

A comparison with predicted data for a series connection, using the analytical model and FE simulations, is also portrayed in the aforementioned figures, as well as in Table 4 to be used as a benchmark. Despite the fact that the analytical model has been reported to produce fairly good results for simpler devices (DuToit and Wardle,

**Table 4.** Comparison of analytical, predicted, and experimental power output in series connection for different resistances.

Resistance (k $\Omega$ )	Analytical data	Finite element data	Experimental data
	Power ( $\mu$ W)	Power ( $\mu$ W)	Power ( $\mu$ W)
30	8.690	5.148	5.88
60	13.868	9.492	12.042
90	16.940	13.119	15.471
130	19.111	16.939	18.243
185	20.157	20.608	21.191
215	20.224	21.99	22.104
250	20.053	22.946	22.09
285	19.712	24.049	21.93
333	19.141	25.089	21.408
444	17.526	22.712	19.867

2007) (Esmaeili and Sousa, 2017), an overestimation of the value of the resonance frequency was obtained in the present case. Hence, a severe under-prediction in power (and voltage) resulted from this modeling approach when considering a frequency for the base excitation of 35.3 Hz. An improved outcome was nonetheless found at a slightly higher frequency, namely, 37 Hz, as illustrated in Figure 10(a) and (b). Contrastingly, owing to the accurate determination of the resonance frequency using the FE modeling, better agreement was obtained with the experimental data when this alternative methodology was applied instead. However, this superior accuracy was reflected by a hundredfold increase in computational cost.

## 7. Conclusions

Measurements of aeroelastic vibrations in a wing prototype with a scalloped (sinusoidal) leading-edge operating in simulated flight conditions in a wind tunnel were carried out employing accelerometers and a laser-Doppler vibrometer. The main findings of these activities are as follows:

- The intense streamwise vortices generated along the upper surface of the wing by the leading-edge modification, designed to deploy the passive stall control mechanism, gave rise to significant vortex-induced vibrations.
- A modal analysis indicated that the measured low-frequency vibrations were consistent with vortex shedding from wings at incidence, giving rise to accelerations in the wing structure up to 0.1 g at an angle of attack of 20°.

A piezoelectric energy harvester was subsequently installed in the scalloped wing prototype with the objective of scavenge energy for a self-powered hybrid passive-active stall control system, taking advantage of the

vortex-induced vibrations. Additional conclusions were drawn from these activities as follows:

- The measurements of extracted power and generated voltage allowed to demonstrate that the proof of concept for a future self-powered hybrid passive-active stall control system was achieved.
- The results have indicated that, with improved design, both the power and the voltage may reach the range required to power lightweight, low-consumption zero-net-mass-flux actuators, in order to generate pulsed synthetic jets for flow control without the need of current rectification.
- The two modeling approaches investigated in this study, namely, analytical modeling and FE simulations, have shown the ability of predicting the electric output from piezoelectric energy harvesting for the intended application.
- Despite its much larger computational cost, the FE approach has proven to produce accurate predictions by adequately addressing the complexities of advanced solutions.

### Declaration of conflicting interests

The author(s) declared no potential conflicts of interest with respect to the research, authorship, and/or publication of this article.

### Funding

The author(s) disclosed receipt of the following financial support for the research, authorship, and/or publication of this article: This work was supported by FCT, through IDMEC, under LAETA, in the framework of project UIDB/50022/2020.

### ORCID iDs

A Esmaeili  <https://orcid.org/0000-0002-4463-6823>  
JMM Sousa  <https://orcid.org/0000-0002-0310-3115>

## References

- Anton SR and Inman DJ (2008) Vibration energy harvesting for unmanned aerial vehicles. In: Ahmadian M (ed), *The 15th International Symposium on: Smart Structures and Materials & Nondestructive Evaluation and Health Monitoring*. International Society for Optics and Photonics, p. 692824.
- Anton S and Sodano H (2007) A review of power harvesting using piezoelectric materials (2003–2006). *Smart Materials and Structures* 16(3): R1–R21.
- Anton SR, Erturk A and Inman DJ (2010) Multifunctional self-charging structures using piezoceramics and thin-film batteries. *Smart Materials and Structures* 19(11): 115021.
- Anton SR, Erturk A and Inman DJ (2012) Multifunctional unmanned aerial vehicle wing spar for low-power generation and storage. *Journal of Aircraft* 49(1): 292–301.
- Câmara JFD and Sousa JMM (2013) Numerical study on the use of a sinusoidal leading edge for passive stall control at low Reynolds number. In: Proc 51st AIAA Aerospace Sciences Meeting. Grapevine, TX, USA.
- Colonus T and Williams DR (2011) Control of vortex shedding on two- and three-dimensional aerofoils. *Philosophical Transactions. Series A, Mathematical, Physical, and Engineering Sciences* 369: 1525–1539.
- De Marqui Junior C, Erturk A and Inman DJ (2009) An electromechanical finite element model for piezoelectric energy harvester plates. *Journal of Sound and Vibration* 327(1–2): 9–25.
- Delgado H, Esmaeili A and Sousa JMM (2014) Stereo PIV measurements of low-aspect-ratio low-Reynolds-number wings with sinusoidal leading edges for improved computational modeling. In: Proc 52nd AIAA Aerospace Sciences Meeting. MD, USA: National Harbor.
- dos Santos CR, Marques FD and Hajj MR (2019) The effects of structural and aerodynamic nonlinearities on the energy harvesting from airfoil stall-induced oscillations. *Journal of Vibration and Control* 25(14): 1991–2007.
- DuToit N and Wardle B (2007) Experimental verification of models for microfabricated piezoelectric vibration energy harvesters. *AIAA Journal* 45(5): 1126–1137.
- Dutoit N, Wardle B and Kim S (2005) Design considerations for MEMS-scale piezoelectric mechanical vibration energy harvesters. *Integrated Ferroelectrics* 71(1): 121–160.
- Elvin NG and Elvin AA (2009) A general equivalent circuit model for piezoelectric generators. *Journal of Intelligent Material Systems and Structures* 20(1): 3–9.
- Erturk A and Inman DJ (2009) An experimentally validated bimorph cantilever model for piezoelectric energy harvesting from base excitations. *Smart Materials and Structures* 18(2): 025009.
- Esmaeili A and Sousa JMM (2017) Power density ratio optimization of bimorph piezocomposite energy harvesters using a multidisciplinary design feasible method. *Composite Structures* 165: 171–179.
- Esmaeili A, Delgado HEC and Sousa JMM (2018) Numerical simulations of low-Reynolds-Number flow past finite wings with leading-Edge protuberances. *Journal of Aircraft* 55(1): 226–238.
- Ewins DJ (2000) *Modal Testing : Theory, Practice, and Application*. Research Studies Press.
- Fatehi P, Mahzoon M, Farid M, et al. (2021) Modal reduction-based finite element method for nonlinear FG piezoelectric energy harvesters. *Journal of Vibration and Control*. Online-First DOI: [10.1177/10775463211048119](https://doi.org/10.1177/10775463211048119).
- Fish FE and Battle JM (1995) Hydrodynamic design of the humpback whale flipper. *Journal of Morphology* 225(1): 51–60.
- Guerreiro JLE and Sousa JMM (2012) Low-Reynolds-number effects in passive stall control using sinusoidal leading edges. *AIAA Journal* 50(2): 461–469.
- Jabbari H, Esmaeili A and Rabizadeh S (2021a) Phase portrait analysis of laminar separation bubble and ground clearance interaction at critical (low) Reynolds number flow. *Ocean Engineering* 238: 109731–109747.
- Jabbari H, Djavarehshkian MH and Esmaeili A (2021b) Static roughness element effects on protuberance full-span wing at micro aerial vehicle application. *Proceedings of the Institution of Mechanical Engineers - Part G*. Online-First DOI: [10.1177/09544100211049932](https://doi.org/10.1177/09544100211049932).
- Li D, Wu Y, Da Ronch A, et al. (2016) Energy harvesting by means of flow-induced vibrations on aerospace vehicles. *Progress in Aerospace Sciences* 86: 28–62.
- Martos D, Delgado HEC and Sousa JMM (2015) Assessment of the potential for micro energy harvesting in a fixed-wing MAV configuration *53rd AIAA Aerospace Sciences Meeting*. Reston, VA, USA.
- Meshki MM, Nobari AS and Sadr MH (2020) A study on nonlinear, parametric aeroelastic energy harvesters under oscillatory airflow. *Journal of Vibration and Control* 28(1–2): 192–202.
- Midé Technology Corporation (2013a) *Piezoelectric Energy Harvester*.
- Midé Technology Corporation (2013b) *Material Properties, Vulture™ Products*.
- Mueller TJ and DeLaurier JD (2003) Aerodynamics of small vehicles. *Annual Review of Fluid Mechanics* 35(1): 89–111.
- Roundy S, Wright P and Rabaey J (2003) A study of low level vibrations as a power source for wireless sensor nodes. *Computer Communications* 26(11): 1131–1144.
- Sawant SG, Deem EA, Agentis DJ, et al. (2015) Chip-scale electrodynamic synthetic jet actuators. In: Proc 28th IEEE International Conference on Micro Electro Mechanical Systems (MEMS). Portugal: Estoril.
- Toprak A and Tigli O (2014) Piezoelectric energy harvesting: state-of-the-art and challenges. *Applied Physics Reviews* 1(3): 031104.
- Xiang J, Wu Y and Li D (2015) Energy harvesting from the discrete gust response of a piezoaeroelastic wing: modeling and performance evaluation. *Journal of Sound and Vibration* 343: 176–193.